1   **Resource limitation modulates the fate of dissimilated nitrogen in a dual-pathway**

2   **Actinobacterium**

3   David C. Vuono[1,6], Robert W. Read[1], James Hemp[2], Benjamin W. Sullivan[3], John A. Arnone

4   III[1], Iva Neveux[1], Bob Blank[4], Carl Staub[5], Evan Loney[1], David Miceli[1], Mari Winkler[6], Romy

5   Chakraborty[7], David A. Stahl[6], Joseph J. Grzymski[1,*]

6   [1]Division of Earth and Ecosystem Sciences, Desert Research Institute, Reno, NV 89512, USA

7   [2]Division of Geological and Planetary Sciences, California Institute of Technology, Pasadena,

8   CA, USA

9   [3]Department of Natural Resources and Environmental Science, University of Nevada, Reno, NV

10   89557, USA

11   [4]Agricultural Research Service, U.S. Department of Agriculture, Reno, NV, 89512, USA

12   [5]Agtron, Inc. 9395 Double R Blvd, Reno, NV 89521, USA

13   [6]Department of Civil and Environmental Engineering, University of Washington, Seattle, WA,

14   98195, USA

15   [7]Lawrence Berkeley National Laboratory, Berkeley, CA, 94729, USA

16   [*]Correspondence: Joseph J. Grzymski, Division of Earth and Ecosystem Sciences, Desert

17   Research Institute, Reno, 2215 Raggio Parkway, NV 89512, USA

18   **Email: Joe.Grzymski@dri.edu**

1

Abstract

20 Respiratory ammonification and denitrification are two evolutionarily unrelated dissimilatory

21 nitrogen (N) processes central to the global N cycle, the activity of which is thought to be

22 controlled by carbon (C) to nitrate (NO_3^-) ratio. Here we find that *Intrasporangium calvum* C5, a

23 novel menaquinone-based dual-pathway denitrifier/respiratory ammonifier, disproportionately

24 utilizes ammonification rather than denitrification when grown under carbon or nitrate limitation,

25 not $C:NO_3^-$ ratio. Instead, $C:NO_3^-$ ratio is a confounding variable for resource limitation. We find

26 that the protein atomic composition for denitrification modules (NirK) are significantly cost

27 minimized for C and N compared to ammonification modules (NrfA), indicating that resource

28 limitation is a major selective pressure imprinted in the architecture of these proteins. The

29 evolutionary precedent for these findings suggests ecological and biogeochemical importance as

30 evidenced by higher growth rates when *I. calvum* grows predominantly using its ammonification

31 pathway and by assimilating its end-product (ammonium) for growth under ammonium-deplete

32 conditions. Genomic analysis of *I. calvum* further reveals a versatile ecophysiology to cope with

33 nutrient stress and redox conditions. Metabolite and transcriptional profiles during growth

34 indicate that transcript abundances encoding for its nitrite reducing enzyme modules, NrfAH and

35 NirK, significantly increase in response to nitrite production. Mechanistically, our results suggest

36 that pathway selection is driven by intracellular redox potential (redox poise), which may be

37 lowered during resource limitation, thereby decreasing catalytic activity of upstream electron

38 transport steps needed for denitrification enzymes. Our work advances our understanding of the

39 biogeochemical flexibility of N-cycling organisms, pathway evolution, and ecological food-

40 webs.

Introduction

42 Globally, respiratory ammonification and denitrification are vital nitrogen (N) dissimilation

43 pathways that either retain reactive N to support net primary productivity or close the N-cycle

44 through the release of gaseous N, respectively [1]. The environmental controls on these two

45 pathways, particularly the ratio of electron-donor to electron-acceptor (e.g., $C:NO_3^-$) [2], have

46 gained attention [3–7] due to increased anthropogenic N inputs into the environment [8].

47 However, the effects of resource limitation on growth and pathway selection (i.e., allocation of C

48   and N to dissimilatory and assimilatory processes), which are often confounded by $C:NO_3^-$ ratio,

49   have not been tested. Strong selective pressures from Earth's shifting biogeochemistry and

50   oxidation-state have driven evolutionary adaptions to microbial electron transport chains (ETC)

51   [9, 10], respiratory chain redox potentials [11–13], and protein atomic composition [14, 15], may

52   shed light on how these pathways are regulated in contemporary organisms. Here, by identifying

53   the biochemical and evolutionary differences between respiratory ammonification and

54   denitrification, we disentangle the ecological significance and molecular mechanisms of electron

55   transfer through either pathway in a dual pathway organism.

56   From a biochemical standpoint, the primary difference between respiratory ammonification and

57   denitrification is their respective source of reducing equivalents in the ETC: 1) heme-based

58   cytochrome c nitrite reductase used in respiratory ammonification receive electrons directly from

59   the quinone (Q) pool [16] while 2) copper and cd_1 nitrite reductases used in denitrification

60   receive electrons from a soluble electron carrier (e.g., cytochrome c) via the bc_1 complex [17].

61   From an evolutionary standpoint, we can place each N-module's origin to a putative time in

62   Earth history based on the metal co-factors that would have been bioavailable: heme-based

63   cytochromes in an ancient, more reduced, environment compared to the copper-containing nitrite

64   reductases in an oxidizing environment [18]. The bioenergetic chains of microorganisms also

65   underwent selective pressure to shift from low-potential (LP) to high-potential (HP) quinones in

66   response to Earth's oxygenation [11, 12]. Menaquinone (MK) is thought to be the ancestral type

67   of LP quinone [19]. Organisms that use ubiquinone (UQ) are thought to have evolved under high

68   O_2 tensions with α-, β-, γ-proteobacteria as the only bacterial clades to use UQ [12]. Surprisingly,

69   our understanding for the biochemistry of denitrification is based predominantly on HP UQ-

70   based systems [20], leaving a significant knowledge gap in the physiology and biochemistry of

71   LP MK-based denitrifiers and how they link electron transfer with energy capture under resource

72   limitation [21–23].

73   In order to resolve the mechanisms of $C:NO_3^-$ control on pathway selection and better understand

74   branched respiratory chains in LP-based nitrate-reducing organisms, we undertook the

75   characterization of the novel Gram-positive Actinobacterium strain *Intrasporangium calvum* C5:

76   a dual-pathway nitrite reducer that uses MK as sole pool quinone. Here we show that over a

77   range of $C:NO_3^-$ ratios, duplicated at two substrate concentrations, *I. calvum* disproportionately

3

78   utilizes its ammonia-forming pathway during C limitation ($\leq$ 0.4mM lactate), when $C:NO_3^-$ ratios

79   are < 1 (an observation contrary to the current paradigm). Using a genome-guided approach

80   coupled to time-series transcriptomics and metabolite profiles, we identified differentially

81   expressed genes in the bacterium's ETC and central metabolic pathways. Using this information

82   to inform a metabolic reconstruction of the ETC and extensive literature on the biochemistry of

83   the bc_1 complex, we propose a new mechanism by which these two pathways are regulated at the

84   biochemical level.

85   **Materials and Methods**

86   **Culture Conditions**

87   <u>Media preparation</u>: All cultures were grown at 30 ºC and shaken at 250 rpm. Nitrate reducing

88   minimal media was prepared with the following final concentrations: NaCl (0.6mM), NH_4Cl

89   (1.75mM) (for ammonium replete conditions but not used in NH4-deplete conditions), MgCl2

90   (0.2mM), CaCl2 (0.04mM), KCl (0.1mM), K2HPO4 (0.01mM), NaHCO3- (0.3mM), cysteine

91   (1mM) as reducing agent, resazurin as redox indicator, and trace elements and trace vitamin

92   solutions as reported [24, 25]. 1M sterile filtered (0.2µm) Concentrated stocks of 60% w/w

93   sodium DL-lactate solution (Sigma-Aldrich, St. Louis, MO, USA), sodium-nitrate and sodium-

94   nitrite ($\geq$99%, Fisher Scientific, Pittsburg, PA, USA) were diluted into media prior to

95   autoclaving to achieve the desired $C:NO_3^-$ ratio. $C:NO_3^-$ ratio was calculated based on [3] where

96   the number of C atoms (n) in the e-donor is multiplied by the concentration of the e-donor,

97   divided by the number of N atoms in the e-acceptor multiplied by the concentration of the e-

98   acceptor (Table S4). See SI Materials and Methods for complete description of Hungate

99   technique prepared media. Mean pH for all culture vessels (time series and end-point; Table S5),

100   measured at the end of each experiment, was 7.3±0.05 (n=144).

101   **Analytical procedures**

102   <u>Growth Curve/Cell counts/Yield Measurements</u>: Growth curves were measured from scratch-

103   free Balch-tubes grown cultures using an automated optical density reader at OD_{600} nm

104   (Lumenautix LLC, Reno, NV). End-point cultures were monitored until all replicates reached

105   stationary phase (65-100 hours depending on $C:NO_3^-$ treatment) (Figure S6). Cell counts were

106   performed by fixing cells in 4% paraformaldehyde (final concentration) for 20 minutes, filtered

4

107 onto 0.2µm pore-sized black polycarbonate filters. A complete description is provided in SI

108 Materials and Methods. Biomass concentrations were measured by filtration and drying as per

109 standard protocol [26]. A complete description is provided in SI Materials and Methods.

110

111 Ion and Gas Chromatography Measurements: A dual channel Dionex ICS-5000+ (Thermo

112 Scientific) ion chromatograph (IC) was used to measure organic (lactate, acetate, and formate)

113 and inorganic (nitrite and nitrate) anions on an AS11-HC column and cations (ammonium) on a

114 CS-16 column from the bacterial growth media. A complete description is provided in SI

115 Materials and Methods.

116 **Phylogenetic, Genomic, and Transcriptomic Analysis**

117 Genomic DNA was assembled using Canu (version 1.7.1) with an estimated genome size of 5

118 million base pairs [27]. The resulting single contiguous fragment was aligned to the *I.* calvum

119 7KIP genome (Acc: NC_014830.1) to compare sequence similarity in Mauve[28, 29]. Genome

120 annotation for C5 was performed through the NCBI Prokaryotic Genome pipeline

121 (www.ncbi.nlm.nih.gov/genome/annotation_prok/). Additional gene prediction analysis and

122 functional annotation was performed by the DOE Joint Genome Institute (JGI) using the Isolate

123 Genome Gene Calling method (Prodigal V2.6.3 February, 2016) under the submission ID

124 172966. The complete genome sequence and annotation is available in the NCBI database under

125 the BioProject number PRJNA475609. A complete description of the phylogenetic, pathway

126 analysis, and cost-minimization calculations is provided in SI Material and Methods. For

127 transcriptomic analysis, the resulting raw reads were inspected using FastQC [30] to determine

128 quality, read length, and ambiguous read percentage. Reads were trimmed based on quality score

129 with a sliding window of 5 base pairs, quality cutoff of 28, trailing cutoff quality score of 10, as

130 well as adapter contamination removal in Trimmomatic [31]. A complete description is provided

131 in SI Materials and Methods. Statistical analyses were conducted in the R environment for

132 statistical computing (r-project.org). Data that was tested using parametric statistical analysis

133 were first validated for normality by visualizing the data as a histogram and testing via Shapiro-

134 Wilks test for normality.

135 **Results**

136   **Genomic analysis of *I. calvum* C5.** We sequenced and analyzed the genome of *I. calvum* C5 to

137   first compare its similarity to the type species *I. calvum* 7KIP. We identified a high degree of

138   sequence similarity to 7KIP based on three homologous sequence regions as locally collinear

139   blocks (SI Results). Genome size of C5 was 4,025,044 base pairs (bp), only 662 bp longer than

140   7KIP. Genomic analysis of the ETC revealed the typical suite of complexes common to

141   facultative aerobes, including primary dehydrogenases (*nuo* complex, succinate dehydrogenase),

142   alternative *NDH-2* NADH dehydrogenase, cytochrome bc_1 complex, high-oxygen adapted

143   cytochrome c oxidase (A-family), and low-oxygen adapted cytochrome *bd* oxidase. The bc_1

144   complex subunits are also located immediately upstream of cytochrome c oxidase, suggesting

145   that these enzymes are encoded in a single operon creating a supercomplex. Despite *I. calvum*'s

146   seeming propensity for aerobic growth on a number of growth media [32], its bioenergetic

147   system uses MK as its sole pool quinone. *I. calvum* also possesses multiple pathways for

148   supplying electrons into the MK-pool, such as formate, malate, hydroxybutyrate, and

149   glycerophosphate dehydrogenases. Once in the MK-pool, there are alternative pathways for

150   MKH_2 oxidation that can circumvent the bc_1 complex, such as a membrane-bound respiratory

151   nitrate reductase module (NarG). In addition, to NarG, its dissimilatory N module composition

152   consists of a truncated denitrification pathway (N_2O is a terminal product) using a copper nitrite

153   reductase NirK and quinol-dependent nitric oxide reductase qNor. *I. calvum* also possesses both

154   catalytic and membrane anchor subunits (NrfA and NrfH, respectively) for a pentaheme

155   cytochrome c module involved in respiratory nitrite ammonification.

156   ***I. calvum* encodes for a functional NrfAH complex and assimilates NH_4^+ via respiratory**

157   **nitrite ammonification.** To gain insight into possible function of the NrfAH complex, we

158   aligned the NrfA protein sequences from C5 and 7KIP to a collection of 33 recognized

159   cytochrome c nitrite reductases from published annotated genomes (Table S1). This confirmed

160   that NrfA from *I. calvum* is a member of the CxxCH 1st heme motif group (Figure 1A), which

161   forms one of four clades on the NrfA phylogenetic tree. We then queried the genomes of the taxa

162   in our phylogeny for other annotated N-reducing modules used in nitrate reduction, nitrite

163   reduction, NO-forming nitrite reduction, and primary pool quinone. Among the three major

164   clades of NrfA, at least 5 additional taxa are noted having dissimilatory N-module inventories

165   containing dual respiratory pathways: *S. thermophilum, B. azotoformans, B. bataviensis*, *B.*

166   *bacteriovorus*, and *Candidatus* N. inopinata, (Figure 1A). None of the taxa in our NrfA

167   phylogeny harbored the cd_1 nitrite reductases (NirS). Due to the exclusive NirK representation in

168   dual-pathway membership, we asked whether there might be differences in protein atomic

169   composition between NirK and NrfA, given the disparate evolutionary origins of these modules

170   [33]. We collected 20 additional publicly available NirK protein sequences from nondual-

171   pathway denitrifiers (Table S1) and calculated the protein C and N composition for our

172   NirK/NrfA collection as atoms per residue side-chain (Figure 1B). These results showed a

173   significant depletion in C and N atoms per residue side-chain (ARSC) for NirK compared to

174   NrfA (C and N: $p<0.001$; t-test), indicating that resource constraints are imprinted on the

175   evolution of these proteins.

176   We next tested the functionality of *I. calvum*'s Nrf complex by growing the bacterium under

177   reducing conditions (8 mM lactate, 12 mM nitrate, ammonium-replete). We then performed a

178   state-transition where biomass from late-exponential growth phase was collected and

179   anaerobically inoculated into ammonia-deplete media (Figure 1C; SI Results). Despite no

180   detectable amounts of ammonium produced in the media over time, cell counts increased

181    $5.4 \times 10^5 \pm 8.9 \times 10^4$ cells/mL (0.126 ± 0.02 optical absorbance at OD_{600}) over a 48-hour incubation,

182   indicating consumption of ammonium produced by NrfA. Net ammonium production was

183   13 ± 2.7 μmoles with the remainder of dissimilated N being used by the denitrification pathway

184   (24 ± 4.2 μmoles N_2O-N), resulting in a recovery of 97.4% dissimilated N. These results

185   confirmed that *I. calvum* C5 has a functional Nrf complex and also consumes the product

186   (ammonium) of respiratory nitrite ammonification.

187   **Respiratory nitrite ammonification exceeds denitrification under C-limitation.** We

188   investigated $C:NO_3^-$ control on respiratory ammonification versus denitrification on cultures of *I.*

189   *calvum* C5 over a high resource $C:NO_3^-$ range (16-0.4 mM lactate, 12 mM nitrate; ratio 4-0.1)

190   and low resource $C:NO_3^-$ range (1.6-0.04 mM lactate, 1.2 mM nitrate; ratio 4-0.1). This

191   experimental design enabled us to evaluate $C:NO_3^-$ control over a broader range than previous

192   studies that only considered ratios ≥ 1.5 [3, 4, 34], while also testing the effects of resource

193   concentration on pathway selection. Under all the treatments tested, gas and ion chromatography

194   measurements showed products of both respiratory pathways, differing only in the relative

195   fraction of N_2O versus ammonium production across treatments (Figure 2). At high resource

196   concentrations, respiratory ammonification did not prevail at high $C:NO_3^-$ ratios (Figure 2A,

7

197   Figure 2B, left panels; Table S2). Instead, significantly greater amounts of N_2O were produced

198   over ammonium, though nitrite was still the major extracellular end-product of nitrate

199   respiration. Despite the predominance of N_2O production under the high resource concentrations,

200   ammonium production exceeded N_2O production only at the lowest $C:NO_3^-$ ratio (0.4 mM

201   lactate, ratio=0.1) (Figure 2) and accounted for 76.2±0.1% of dissimilated N.

202   Results from the low resource dataset provided weak support for the strict stoichiometry

203   hypothesis that $C:NO_3^-$ controls pathway selection. Ammonia exceeded N_2O production only

204   under one high $C:NO_3^-$ ratio treatment (ratio=4; 1.6 mM lactate; Figure 2A, Figure 2B, right

205   panels). However, at ratios ≤1 (≤0.4 mM lactate), significantly more ammonium than N_2O was

206   produced. On average, respiratory ammonification accounted for 78.1±8.9% of dissimilated N

207   for lactate concentrations ≤0.4 mM. When these results are taken in context with cell physiology,

208   we observed a significant and positive relationship between specific growth rate (μ) and the

209   fraction of N dissimilated by respiratory ammonification (R^2=0.5; p<0.001) (Figure 2C, S1;

210   Table S3).

211   **Resource concentration influences the metabolite profiles of ammonium and N_2O**

212   **production.** Given the co-occurrence of end products from both pathways during the end-point

213   experiments (Figure 2), we next investigated the timing of ammonium and N_2O production

214   relative to metabolite profiles for lactate, nitrate/nitrite, and growth phase at two resource

215   concentrations with the same ratio (8 mM and 0.8 mM lactate, ratio=2; Figure 1A, Figure S2,

216   Figure S3). Despite ample e-donor and e-acceptor available for growth, the high resource

217   cultures entered a quasi-stationary phase at ~50 hours, after which there was continued slow

218   growth (Figure 1A). Metabolite profiles showed that ammonium and N_2O production began

219   simultaneously, as soon as nitrite was produced from nitrate reduction. The low resource cultures

220   entered stationary phase at ~40 hours (Figure S2) after nitrate had been fully utilized. No further

221   cell growth was observed after stationary phase was reached. These results show that cell growth

222   occurred primarily on the reduction of nitrate, while nitrite reduction to ammonium and N_2O

223   occurred during a stationary growth phase, demonstrating that microbial activity is not always

224   correlated with growth. The metabolite profiles for ammonium and N_2O at low resources (Figure

225   S2) did not mirror those observed at high resources (Figure 2A). The rate of N_2O production

226   significantly decreased and ammonium production oscillated rather than steadily increase

227   through time. These differences in metabolite profiles, further demonstrate that concentration

228   influences the activities of pathway bifurcation. Repeated time series experiments that were

229   extended up to 300 hours show that nitrite is slowly depleted, but does not get fully consumed

230   (Figure S3). When cultures were given nitrite, instead of nitrate as a terminal electron acceptor (8

231   mM lactate, 12 mM nitrite; ratio=2), we observed no immediate growth (as was observed with

232   nitrate) but measured more N_2O than ammonium production (33.4±4.8 μmoles N_2O-N and

233   8.0±2.5 μmoles NH_4^+, respectively) (Figure S4), demonstrating respiratory ammonification does

234   not exceed denitrification when nitrite is supplied as the sole acceptor in *I. calvum*.

235   **Nitrite-reducing modules are up-regulated during late exponential- and stationary-phase**

236   **growth.** In order to gain insight into mechanisms of gene regulation and transcriptional

237   organization of *I. calvum*, we conducted RNA-Seq in parallel with the high resource time-series

238   metabolite profile (Figure 3A). This approach enabled us to compare genome-wide differential

239   expression based on $\log_2$ fold change (lfc) of RNA extracted from three growth phases: early

240   exponential (EE), late exponential (LE), and stationary (ST) (Figure 3B, Figure S5). Within the

241   central metabolic pathway beginning with the conversion of lactate to pyruvate, we observed a

242   moderate decrease in transcript abundance of L-lactate dehydrogenase (LDH) (Intca_16740)

243   between EE-LE and -ST (lfc = -1.6±0.7; -1.9±0.7), respectively. Lactate utilization protein C

244   (LUP) (Intca_04080), an enzyme involved in lactate degradation, also showed a moderate and

245   significant decrease in transcript abundance between EE-LE and -ST (lfc = -1.6±0.6; -2.4±0.6,

246   *p*=0.002), respectively. *I. calvum* encodes for two parallel metabolic pathways for pyruvate

247   conversion to acetyl-CoA: pyruvate dehydrogenase (PDH) (Intca_01255) and pyruvate

248   ferredoxin oxidoreductase (PFOR) (Intca_15510). For PDH, there was a significant and

249   moderate increase in transcript abundance between EE-LE and -ST (lfc = 2.1±0.6, *p*=0.002;

250   1.5±0.6), respectively. For PFOR, there was a minor decrease in transcript abundance between

251   EE-LE (lfc = -0.43±0.5), and then a moderate increase in transcript abundance between EE-ST

252   (1.1±0.5). Citrate synthase (Intca_04135), the enzyme catalyzing the conversion of acetyl-CoA

253   to citrate and the first step of the tricarboxylic acid (TCA) cycle, showed a highly significant

254   increase in transcript abundance between EE-LE and -ST (lfc = 4.3±0.5, *p*<0.001; 6.9±0.5,

255   *p*<0.001).

256   Within the ETC, there was moderate and significant decrease in transcript abundance for all

257   subunits from the primary dehydrogenase (*nuo* complex; Intca_03465-03539) between EE-LE

258   and -ST (lfc = -1.2±0.3; -2.4±0.6, *p*<0.001), respectively. Nitrate reductase subunits showed no

259   change in transcript abundance between EE-LE (lfc = 0.01±0.07) and moderately decreased in

260   abundance by ST (lfc = -1.2±0.1), which was corroborated by the depletion of nitrate during

261   stationary phase. There was a significant increase in transcript abundance of *nirK* (Intca_17170)

262   (lfc = 2.2±0.6, *p*=0.003; 2.4±0.6, *p*<0.001) and quinol dehydrogenase/membrane anchor subunit

263   *nrfH* (Intca_09465) (lfc = 2.5±0.6, *p*=0.001; 2.1±0.6, *p*=0.003) by EE-LT and EE-ST,

264   respectively, which coincided with nitrite production (Figure 3A). The catalytic subunit of the

265   cytochrome c nitrite reductase complex (*nrfA*) (Intca_09460) also increased moderately in

266   transcript abundance by EE-LT and EE-ST (lfc = 1.6±0.6; 1.0±0.6), respectively (Figure 3B).

267   Contrary to the transcript abundance patterns of *nirK* and *nrfAH*, nitric oxide reductase (qNor;

268   Intca_01525) transcripts moderately increased between EE-LT (lfc = 1.6±0.6) but decreased in

269   the successive time periods (lfc = 0.43±0.6 between EE-ST; lfc = -1.2±0.6 between LE-ST)

270   (Figure 3B).

271   There was a significant increase in transcript abundance of formate transporter *focA*

272   (Intca_17150) between EE-ST, as well as LE-ST (lfc = 4.9±0.7, *p*=0.002; 4.8±0.7, *p*=0.002;

273   respectively). We verified the production of formate in our ion chromatography measurements in

274   the range of 100-200μM following late exponential growth. We also observed a moderate

275   increase in transcript abundance of formate dehydrogenase (FDH) subunits (Intca_11150-

276   11160). These results implicate the activity of formate oxidation, which would contribute to a Δ*p*

277   in the periplasm via a Q-loop mechanism and the reduction of MK for electron transfer to nitrite

278   via cytochrome c nitrite reductase. Considering that formate was not provided in our media

279   recipe, an alternative pathway for formate production must exist in *I. calvum*. We also observed

280   acetate production in similar concentrations as formate (100-200μM). In *E. coli*, formate is

281   produced anaerobically from the action of pyruvate formate lyase (PFL). We identified a putative

282   PFL based on genome annotation (Intca_12230), where transcript abundance also significantly

283   increased by ST. PFL is also highly sensitive to oxygen [35], which was also in agreement with a

284   significant increase in transcript abundance between EE-ST and LE-ST (Figure 3B) of

285   cytochrome *bd* oxidase (Intca_01110 and Intca_01115), which is thought to protect anaerobic

286   enzymes against oxidative stress [36].

10

Discussion

288   We challenge the paradigm that $C:NO_3^-$ ratio controls pathway selection in a dual-pathway

289   organism based on a simple principle: ratios do not account for the abundance of growth-limiting

290   resources. We hypothesized that limitation in C or NO_3^- should better predict pathway selection

291   in a dual-pathway denitrifier/respiratory ammonifier. To test this hypothesis, we systematically

292   measured the response of the Gram-positive Actinobacterium *Intrasporangium calvum* C5 to the

293   same range of $C:NO_3^-$ ratios at both high and low resource loadings to better resolve mechanisms

294   of pathway selection. We demonstrated that resource concentration, not $C:NO_3^-$ ratio, influences

295   pathway selection. We found stronger support for respiratory ammonification preference under

296   C-limitation (at low $C:NO_3^-$ ratios), which also grew at significantly higher growth rates (Figure

297   2). These results suggest that the NrfA complex, which receives electrons directly from the MK-

298   pool, is optimized to maximize power when one or more resources are limiting. The enrichment

299   of C and N ARSC in publically available NrfA over NirK protein seuqences (Figure 1B)

300   provides further support and evolutionary precedence to ammonification preference over

301   denitrification under resource limitation. This is because the end-product of ammonification can

302   be used as an assimilatory N-source (Figure 1C), indicating no evolutionary constraint to cost

303   minimize N. These data, together with metabolic reconstructions from metabolite and

304   transcriptional profiles (Figure 3), suggest that $C:NO_3^-$ ratio alone is insufficient to explain

305   pathway selection.

306   The theoretical basis for pathway selection is explained by the law of the minimum (LM) and the

307   maximum power principle (MPP), which state that growth is limited by the least abundant

308   resource and that biological systems are designed to maximize power in order to effectively

309   allocate energy to reproduction and survival [37, 38], respectively. Here, it appears these two

310   theories are working together: when resources are limited, the cell utilizes the respiratory

311   pathway for growth that is optimized to maximize power. Power, in this case, is realized as

312   higher growth rates from the cultures exhibiting disproportionately higher ammonium production

313   than N_2O production (Figure 2: high resources: $C:NO_3^-$ ratio = 0.1; low resources: $C:NO_3^-$ ratios

314   = 4, 1, 0.5, 0.1). More specifically, the bacterium must generate a greater Δp in order to

315   maximize power when starved for a growth limiting resource. This may help to further explain

316   how respiratory ammonification, which is overall energetically less favorable than denitrification

11

317   (lactate with nitrite: $\Delta G° = -763.98$ versus $\Delta G° = -1196.93$, respectively), can have higher growth

318   yields [39] and growth rates (Figure 2, Figure S1) under C- and N-limitation due to the higher

319   energy yield on a per-nitrite basis (denitrification: -217 KJ per mole nitrite; respiratory

320   ammonification: -399 KJ per mole nitrite). For comparison, a total of 8 H^+ are translocated

321   during denitrification by *I. calvum* (not including nitrate reduction since both pathways share this

322   step) (Figure 3): NADH dehydrogenase translocates 4 H^+ per MKH_2 oxidized and the bc_1

323   complex translocates an additional 4 H^+ per MKH_2 oxidized. However, 2 H^+ must be consumed

324   in the periplasm to reduce nitrite to NO [40]. qNor has a net zero H^+ release (consumes 2 H^+ to

325   make N_2O but releases 2 H^+) without MKH_2 regeneration [41]. Thus, a net total of 6 H^+ are

326   translocated per nitrite reduced in denitrification with added biosynthetic costs of making the bc_1

327   complex and qNor. In respiratory ammonification, MK/MKH_2 redox pair is cycled between

328   NADH dehydrogenase and formate dehydrogenase. 6 electrons and 8 H^+ are needed to reduce

329   nitrite to ammonium, thus 3 MKH_2 are needed [16]. If MKH_2 is received from NADH

330   dehydrogenase, 12 H^+ are translocated plus 2 H^+ from FDH. As each MKH_2 is oxidized at the

331   binding site of NrfH, 2 H^+ are liberated [16], resulting in a net total of 12 H^+ translocated per

332   nitrite reduced for respiratory ammonification. This implies that the cell might deplete its NADH

333   pool more rapidly on a per nitrite basis. However, if more protons are pumped in the early stages

334   of growth, the cell would be allocating the ATP generated for anabolism, as evidenced by higher

335   growth rates in the cultures exhibiting higher amounts of respiratory ammonification (Figure 2),

336   which is supported by the MPP.

337   Under our high resource conditions (Figure 2; left panels), at $C:NO_3^-$ ratios ≥ 1, we observed that

338   denitrification prevailed and these cultures had lower growth rates than the predominantly

339   ammonium producing cultures. These high resource circumstances resulted in the production of

340   toxic intermediates (i.e., NO_2^- and possibly NO, albeit at undetectable levels), which may explain

341   why these cultures had lower growth rates (Figure 2; left panels) and quasi-steady state growth

342   curves in our high resource metabolite profile (Figure 3A). Rowley and colleagues [42] reported

343   that at least 20% of the N_2O released during high C conditions were produced by competition

344   between nitrite and nitrate in the active-site of NarG. Under excess C concentrations, NarG

345   produces intracellular NO from NO_2^- and these intermediates are likely inhibitory to cell growth,

346   which may explain why our growth curves (Figure 3A) reached a quasi-steady state before

347   nitrate had been fully utilized (as compared to the low resource metabolite profile, Figure S2).

348   Furthermore, resources were not limiting growth under these conditions. Rather, the cells were

349   likely experiencing toxicity from NO and NO_2^- and thus the metabolic outcomes would be

350   beyond the scope of the LM and MPP. Nonetheless, these results clearly demonstrate that end-

351   product formation from the two resource concentrations tested, with the same $C:NO_3^-$ ratios, are

352   not identical thereby refuting the $C:NO_3^-$ control hypothesis.

353   We selected a single treatment (8 mM lactate, 12 mM nitrate; $C:NO_3^-$ ratio = 2), in which we

354   observed both denitrification and respiratory ammonification occurring simultaneously, for

355   RNA-Seq in order to gain insight into the transcriptional organization of actively growing *I.*

356   *calvum* cells (Figure 3). Strangely, we saw a decrease in transcript abundance encoding for two

357   enzymes known to convert lactate to pyruvate, LDH and LUP. While normalized read counts

358   (Figure S5) were generally consistent across growth phases, indicative of constitutive expression,

359   further research investigating the mode of anaerobic lactate oxidation in *I. calvum* would

360   illuminate how reducing equivalents are fed into its central metabolic pathway. For example, *S.*

361   *loihica* PV-4 is known to use lactate for both denitrification and respiratory ammonification, but

362   only uses acetate for denitrification [24]. Nonetheless, our transcriptomic data suggests that

363   pyruvate plays a central role in providing reducing equivalents to the TCA cycle as Acetyl-CoA,

364   as evidenced by significant upregulation in the genes encoding for pyruvate dehydrogenase and

365   citrate synthase, as well as apparent "leaking" via incomplete lactate oxidation through the

366   release of acetate and formate. Such leaking may be produced by a putative PFL, adding to the

367   diversity of C utilization pathways feeding the ETC, and thereby driving pathway selection for

368   nitrite reduction. Our transcriptomic results, coupled with a parallel metabolite profile (Figure 3),

369   also suggest that the dual-pathway is induced by the presence of nitrite, and is not constitutively

370   expressed like nitrate reductase, *narG*. Furthermore, it appears that the significant increase in

371   transcript abundance for the gene encoding the *bd* oxidase helps to protect the anaerobic-

372   dependent biochemical machinery against oxidative stress, thereby scavenging any residual

373   oxygen during anaerobic growth.

374   Our metabolite profiles for N oxyanion respiration and N_2O versus ammonium production show

375   conflicting patterns relative to previous studies (Figure 3A, Figure S2). Yoon and colleagues [43]

376   reported complete reduction of nitrate, production of nitrite, and then rapid consumption of

377   nitrite, with N_2O as the main end-product, by *S. loihica* PV-4 (5 mM lactate, 1 mM nitrate;

13

378   ratio=0.6). When Yoon and colleagues [43] replaced nitrate with nitrite as the dominant electron

379   acceptor (5 mM lactate, 1 mM nitrite, ratio=0.6), ammonification prevailed. Other research has

380   shown the same response to nitrite replacement and ammonification dominance using non-

381   fermentable C-sources (i.e., acetate) in chemostat enrichments of *Geobacter lovleyi*[44]. In our

382   work, nitrite was never fully depleted (Figure 3A, Figure S2, Figure S3) and when nitrite was

383   given as the only electron acceptor, the bacterium predominantly used denitrification but without

384   concurrent growth (Figure S4). Similar to our work, Kraft and colleagues[34] also reported

385   denitrification dominance when nitrite was supplied as the terminal acceptor. These differences

386   highlight an incomplete understanding for the molecular mechanisms underlying the framework

387   put forth by the LM and MPP.

388   A detailed look into the biochemistry of ETC complexes helps to shed light on the molecular

389   mechanisms modulating pathway bifurcation. For example, Yoon and colleagues [3]

390   demonstrated that elevated pH selects for ammonification in *S. loihica* PV-4. This phenotypic

391   response is due to a decrease in the midpoint potential of the Rieske protein at higher pH [45–

392   48]. Thus, any hindrance of electron flow through the bc_1 complex would ultimately reduce the

393   activity of downstream processes and promote alternative respiratory pathways. Nitrogen and C

394   limitation have also been shown to influence flux distributions in redox sensitive proteins,

395   including those found in electron transport [49]. A drop in the intracellular redox potential (redox

396   poise) of the cell due to resource limitation may decrease the midpoint potential of the Rieske

397   protein and reduce the activity of any downstream electron exit modules, such as NirK [50–52].

398   Thus, based on fundamental principles of protein redox chemistry and thermodynamics, it

399   becomes clear that denitrification versus ammonification are likely not modulated by an arbitrary

400   ratio of $C:NO_3^-$, but rather by thermodynamic constraints of the Q-cycle [11, 12]. The phenotypic

401   response of higher rates of denitrification over ammonification at high $C:NO_3^-$ ratios in other

402   published studies [3, 4] may also be due to enrichment bias for organisms that utilize quinones

403   with higher midpoint potentials in their bioenergetic chains (Figure 1). Bergdoll and colleagues

404   [11] suggested that comparisons of Rieske/cyt*b* complexes from organisms with high- and low-

405   potential quinones may help to reconcile the thermodynamic properties of Q-cycle function.

406   However, most of our understanding of denitrification bioenergetics is based on evolutionarily

407   recent UQ-based HP bioenergetic chains from Gram-negative *α*-, *β*-, *γ*-proteobacteria. Because *I.*

14

408   *calvum* uses a MK-based LP bioenergetic chain it may be possible that the differences in

409   pathway selection across treatments are unique to LP chains.

410   Piecing together the evolutionary history of the N-cycle using isotopic signatures for

411   geochemically available N module cofactors (i.e., Ni, Fe, and Mo) coupled to molecular

412   evolutionary analysis has revealed respiratory ammonification was likely a major component of

413   the Archean N-cycle [33]. Abiotic nitrite formation and depletion of ammonia through

414   photodissociation [53] would have created selective pressures for a dissimilatory N pathway that

415   also produced assimilatory N. We demonstrate that NrfA proteins are significantly enriched in N

416   compared to NirK (i.e., no evolutionary constraints to cost minimize N in the *nrfA* gene product

417   [15]) (Figure 1B) and that ammonium production (without accumulation in the medium)

418   supports growth in *I. calvum* (Figure 1C). The Nrf module is also relatively simplistic in that it

419   receives electrons directly from the quinol pool and not the bc_1 complex used in denitrification.

420   The early exit of electrons from the ETC (i.e., before reaching the bc_1 complex) suggests that Nrf

421   may have originated prior to the bc_1 complex. Furthermore, the quinol oxidation site (Q_o) of

422   cytochrome *b* contains a PDWY motif, indicative of an ancestral LP respiratory chain found in

423   many Gram-positive organisms [54]. However, there is still debate regarding the presence of a

424   cytochrome *bc* complex in the last universal common ancestor [54, 55]. Lastly, the Nrf module is

425   wired to operate via a q-loop with formate dehydrogenase whose Mo-cofactors would have also

426   been bioavailable during the Archean, further supporting an early evolution.

427   In summary, we employ a new predictive framework that accounts for the biochemistry and

428   evolutionary history of N modules, ETC complexes, and pool quinones to suggest the

429   mechanisms by which these two pathways are regulated at the molecular level. With this

430   understanding, it may be possible to extend our framework to environmental microbial

431   populations and accelerate model development across different ecosystem scales (i.e., cross-scale

432   systems biology).

442   **Competing Interests**

443   The authors declare no conflicts of interest

444   **References**

445   1.   Knowles R. Denitrification. *Microbiol Rev* 1982; **46**: 43–70.

446   2.   Tiedje JM, Sexstone AJ, Myrold DD, Robinson JA. Denitrification: ecological niches , competition and
447   survival. *Antonie Van Leeuwenhoek* 1982; **48**: 569–583.

448   3.   Yoon S, Cruz-García C, Sanford R, Ritalahti KM, Löffler FE. Denitrification versus respiratory
449   ammonification: Environmental controls of two competing dissimilatory NO 3-/NO 2-reduction pathways in
450   Shewanella loihica strain PV-4. *ISME J* 2015; **9**: 1093–1104.

451   4.   van den Berg EM, van Dongen U, Abbas B, van Loosdrecht MC. Enrichment of DNRA bacteria in a
452   continuous culture. *ISME J* 2015; **9**: 2153–2161.

453   5.   Schmidt CS, Richardson DJ, Baggs EM. Constraining the conditions conducive to dissimilatory nitrate
454   reduction to ammonium in temperate arable soils. *Soil Biol Biochem* 2011; **43**: 1607–1611.

455   6.   Hardison AK, Algar CK, Giblin AE, Rich JJ. Influence of organic carbon and nitrate loading on partitioning
456   between dissimilatory nitrate reduction to ammonium (DNRA) and N2 production. *Geochim Cosmochim*
457   *Acta* 2015; **164**: 146–160.

458   7.   Fazzolari É, Nicolardot B, Germon JC. Simultaneous effects of increasing levels of glucose and oxygen
459   partial pressures on denitrification and dissimilatory nitrate reduction to ammonium in repacked soil cores.
460   *Eur J Soil Biol* 1998; **34**: 47–52.

461   8.   Galloway JN, Aber JD, Erisman JW, Seitzinger SP, Howarth RW, Cowling EB, et al. The Nitrogen
462   Cascade. *Bioscience* 2003; **53**: 341.

463   9.   Moparthi VK, Hägerhäll C. The evolution of respiratory chain complex i from a smaller last common
464   ancestor consisting of 11 protein subunits. *J Mol Evol* 2011; **72**: 484–497.

465   10.   Dibrova D V., Cherepanov DA, Galperin MY, Skulachev VP, Mulkidjanian AY. Evolution of cytochrome
466   bc complexes: From membrane-anchored dehydrogenases of ancient bacteria to triggers of apoptosis in
467   vertebrates. *Biochim Biophys Acta - Bioenerg* 2013; **1827**: 1407–1427.

468   11.   Bergdoll L, Ten Brink F, Nitschke W, Picot D, Baymann F. From low- to high-potential bioenergetic chains:
469   Thermodynamic constraints of Q-cycle function. *Biochim Biophys Acta* 2016; **1857**: 1569–1579.

470   12.   Schoepp-Cothenet B, Lieutaud C, Baymann F, Verméglio A, Friedrich T, Kramer DM, et al. Menaquinone
471   as pool quinone in a purple bacterium. *Proc Natl Acad Sci* 2009; **106**: 8549–54.

472   13.   Soo RM, Hemp J, Parks DH, Fischer WW, Hugenholtz P. On the origins of oxygenic photosynthesis and
473   aerobic respiration in Cyanobacteria. *Science (80-)* 2017; **355**: 1436–1440.

474   14.   Baudouin-Cornu P, Schuerer K, Marlière P, Thomas D. Intimate evolution of proteins: Proteome atomic
475   content correlates with genome base composition. *J Biol Chem* 2004; **279**: 5421–5428.

476   15.   Grzymski JJ, Dussaq AM. The significance of nitrogen cost minimization in proteomes of marine
477   microorganisms. *ISME J* 2012; **6**: 71–80.

478   16.   Einsle O, Messerschmidt A, Huber R, Kroneck PMH, Neese F. Mechanism of the six-electron reduction of
479   nitrite to ammonia by cytochrome c nitrite reductase. *J Am Chem Soc* 2002; **124**: 11737–11745.

480   17.   Kraft B, Strous M, Tegetmeyer HE. Microbial nitrate respiration - Genes, enzymes and environmental
481   distribution. *J Biotechnol* 2011; **155**: 104–117.

482   18.   Godfrey L V., Falkowski PG. The cycling and redox state of nitrogen in the Archaean ocean. *Nat Geosci*
483   2009; **2**: 725–729.

484   19.   Nitschke W, Dracheva S. Reaction center associated cytochromes in Anoxygenic Photosynthetic Bactera.
485   In: Blankenship R, Madigan M, Bauer C (eds).1995. Kluwer Academic, Dordrecht, The Netherlands, pp
486   775–805.

487   20.   Lalucat J, Bennasar A, Bosch R, Garcia-Valdes E, Palleroni NJ. Biology of Pseudomonas stutzeri.
488   *Microbiol Mol Biol Rev* 2006; **70**: 510–547.

489   21.   Suharti, de Vries S. Membrane-bound denitrification in the Gram-positive bacterium Bacillus azotoformans.
490   *Biochem Soc Trans* 2005; **33**: 130–133.

491   22.   Heylen K, Keltjens J, Stein LY. Redundancy and modularity in membrane-associated dissimilatory nitrate
492   reduction in Bacillus. *Front Microbiol* 2012; **3**: 1–27.

493   23.   Decleyre H, Heylen K, Bjorn T, Willems A. Highly diverse nirK genes comprise two major clades that
494   harbour ammonium-producing denitrifiers. *BMC Genomics* 2016; **17**: 1–13.

495   24.   Yoon S, Sanford RA, Löffler FE. Shewanella spp. Use acetate as an electron donor for denitrification but
496   not ferric iron or fumarate reduction. *Appl Environ Microbiol* 2013; **79**: 2818–2822.

497   25.   Hillesland KL, Lim S, Flowers JJ, Turkarslan S, Pinel N, Zane GM, et al. Erosion of functional
498   independence early in the evolution of a microbial mutualism. *Proc Natl Acad Sci* 2014; **111**: 14822–14827.

499   26.   APHA. Standard Methods for the Examination of Water and Wastewater, 23rd ed. 2012. American Public
500   Health Association: Washington, DC.

501   27.   Koren S, Walenz BP, Berlin K, Miller JR, Bergman NH, Phillippy AM. Canu : scalable and accurate long- -
502   - read assembly via adaptive k - - - mer weighting and repeat separation. *Genome Res* 2017; 1–35.

503   28.   Darling ACE, Mau B, Blattner FR, Perna NT. Mauve : Multiple Alignment of Conserved Genomic
504   Sequence With Rearrangements. *Genome Res* 2004; **14**: 1394–1403.

505   29.   Darling AE, Mau B, Perna NT. Progressivemauve: Multiple genome alignment with gene gain, loss and
506   rearrangement. *PLoS One* 2010; **5**: e11147.

507   30.   Andrews S. FastQC: A quality control tool for high throughput sequence data. *Available online at: http://*
508   *www.bioinformatics.babraham.ac.uk/projects/fastqc* 2010.

509   31.   Bolger AM, Lohse M, Usadel B. Trimmomatic: A flexible trimmer for Illumina sequence data.
510   *Bioinformatics* 2014; **30**: 2114–2120.

511   32.   Kalakoutskii LV, Kirillova IP, Krassilnikov NA. a New Genus of the. *J Gen Microbiol* 1967; **48**: 373-79–
512   85.

513   33.   Klotz MG, Stein LY. Nitrifier genomics and evolution of the nitrogen cycle. *FEMS Microbiol Lett* 2008;
514   **278**: 146–156.

34. Kraft B, Tegetmeyer HE, Sharma R, Klotz MG, Ferdelman TG, Hettich RL, et al. The environmental controls that govern the end product of bacterial nitrate respiration. *Science (80-)* 2014; **345**: 676–679.

35. Abbe KS, Takahashi S, Yamada T. Invovlement of oxygen-sensitive pyruvate-formate lysase in mixed-acid fermetnation by Streptococcus mutans under strictly anaerobic conditions. *J Bacteriol* 1982; **152**: 175.

36. Das A, Silaghi-Dumitrescu R, Ljungdahl LG, Kurtz DM. Cytochrome *bd* oxidase, oxidative stress, and dioxygen tolerance of the strictly anaerobic bacterium *Moorella thermoacetica*. *J Bacteriol* 2005; **187**: 2020–2029.

37. Lotka AJ. Contribution to the Energetics of Evolution. *Proc Natl Acad Sci* 1922; **8**: 147–151.

38. DeLong JP. The maximum power principle predicts the outcomes of two-species competition experiments. *Oikos* 2008; **117**: 1329–1336.

39. Strohm TO, Griffin B, Zumft WG, Schink B. Growth yields in bacterial denitrification and nitrate ammonification. *Appl Environ Microbiol* 2007; **73**: 1420–1424.

40. Zumft WG. Cell biology and molecular basis of denitrification. *Microbiol Mol Biol Rev* 1997; **61**: 533–616.

41. Hemp J, Gennis RB. Diversity of the Heme-Copper Superfamily in Archaea: Insights from Genomics and Structural Modeling. In: Schäfer G, Penefsky HS (eds). *Results and Problems in Cell Differentiation*. 2008. Springer Science+Business Media, pp 1–28.

42. Rowley G, Hensen D, Felgate H, Arkenberg A, Appia-ayme C, Prior K, et al. Resolving the contributions of the membrane-bound and periplasmic nitrate reductase systems to nitric oxide and nitrous oxide production in Salmonella enterica serovar Typhimurium. *Biochem J* 2012; **762**: 755–762.

43. Yoon S, Sanford RA, Löffler FE. Nitrite control over dissimilatory nitrate/nitrite reduction pathways in Shewanella loihica strain PV-4. *Appl Environ Microbiol* 2015; **81**: 3510–3517.

44. van den Berg EM, Rombouts JL, Kuenen JG, Kleerebezem R, van Loosdrecht MCM. Role of nitrite in the competition between denitrification and DNRA in a chemostat enrichment culture. *AMB Express* 2017; **7**: 1–7.

45. Link TA, Hagen WR, Pierik AJ, Assmann C, von Jagow G. Determination of the redox properties of the Rieske cluster of bovine heart bc1 complex by direct electrochemistry of a water- soluble fragment. *EurJBiochem* 1992; **208**: 685–691.

46. Ugulava NB, Crofts AR. CD-monitored redox titration of the Rieske Fe-S protein of Rhodobacter sphaeroides: pH dependence of the midpoint potential in isolated bc1 complex and in membranes. *FEBS Lett* 1998; **440**: 409–413.

47. Zu Y, Couture MMJ, Kolling DRJ, Crofts AR, Eltis LD, Fee JA, et al. Reduction Potentials of Rieske Clusters: Importance of the Coupling between Oxidation State and Histidine Protonation State. *Biochemistry* 2003; **42**: 12400–12408.

48. Trumpower BL. Cytochrome bc1 complexes of microorganisms. *Microbiol Rev* 1990; **54**: 101–129.

49. Ansong C, Sadler NC, Hill EA, Lewis MP, Zink EM, Smith RD, et al. Protein redox dynamics during light-to-dark transitions in cyanobacteria and impacts due to nutrient limitation. *Front Microbiol* 2014; **5**: 1–10.

50. Snyder CH, Merbitz-Zahradnik T, Link TA, Trumpower BL. Role of the Rieske Iron – Sulfur Protein Midpoint Potential in the Protonmotive Q-Cycle Mechanism of the Cytochrome bc 1 Complex. *J Bioenerg Biomembr* 1999; **31**: 235–242.

51. Denke E, Merbitz-Zahradnik T, Hatzfeld OM, Snyder CH, Link TA, Trumpower BL. Alteration of the midpoint potential and catalytic activity of the Rieske iron-sulfur protein by changes of amino acids forming

556   hydrogen bonds to the iron-sulfur cluster. *J Biol Chem* 1998; **273**: 9085–9093.

557   52.   Hunte C, Solmaz S, Palsdóttir H, Wenz T. A structural perspective on mechanism and function of the
558   cytochrome bc1 complex. In: Schäfer G, Penefsky HS (eds). *Results and Problems in Cell Differentiation*.
559   2008. Springer Science+Business Media, pp 253–270.

560   53.   Falkowski PG. Evolution of the nitrogen cycle and its influence on the biological sequestration of CO2 in
561   the ocean. *Nature* 1997; **387**: 272–275.

562   54.   Kao WC, Hunte C. The molecular evolution of the Qo Motif. *Genome Biol Evol* 2014; **6**: 1894–1910.

563   55.   Dibrova D V., Cherepanov DA, Galperin MY, Skulachev VP, Mulkidjanian AY. Evolution of cytochrome
564   bc complexes: From membrane-anchored dehydrogenases of ancient bacteria to triggers of apoptosis in
565   vertebrates. *Biochim Biophys Acta - Bioenerg* 2013; **1827**: 1407–1427.

566   56.   White D. The physiology and biochemistry of prokaryotes, 3rd ed. 2000. Oxford University Press.

567   57.   Thauer RK, Jungermann K, Decker K. Energy conservation in chemotrophic anaerobic bacteria. *Bacteriol*
568   *Rev* 1977; **41**: 100–180.

569   58.   Giardina CP, Ryan MG. Total belowground carbon allocation in a fast-growing Eucalyptus plantation
570   estimated using a carbon balance approach. *Ecosystems* 2002; **5**: 487–499.

571   59.   Edgar RC. MUSCLE: multiple sequence alignment with high accuracy and high throughput. *Nucleic Acids*
572   *Res* 2004; **32**: 1792–7.

573   60.   Tamura K, Peterson D, Peterson N, Stecher G, Nei M, Kumar S. MEGA5: Molecular evolutionary genetics
574   analysis using maximum likelihood, evolutionary distance, and maximum parsimony methods. *Mol Biol*
575   *Evol* 2011; **28**: 2731–2739.

576   61.   Stamatakis A. RAxML version 8: A tool for phylogenetic analysis and post-analysis of large phylogenies.
577   *Bioinformatics* 2014; **30**: 1312–1313.

578   62.   Kelley LA, Mezulis S, Yates C, Wass M, Sternberg M. The Phyre2 web portal for protein modelling,
579   prediction, and analysis. *Nat Protoc* 2015; **10**: 845–858.

580   63.   Dobin A, Davis CA, Schlesinger F, Drenkow J, Zaleski C, Jha S, et al. STAR: Ultrafast universal RNA-seq
581   aligner. *Bioinformatics* 2013; **29**: 15–21.

582   64.   Liao Y, Smyth GK, Shi W. FeatureCounts: An efficient general purpose program for assigning sequence
583   reads to genomic features. *Bioinformatics* 2014; **30**: 923–930.

584   65.   Love MI, Huber W, Anders S. Moderated estimation of fold change and dispersion for RNA-seq data with
585   DESeq2. *Genome Biol* 2014; **15**: 1–21.

586

Figure legends

Figure 1. (A) Maximum likelihood phylogenetic tree of NrfA amino acid sequences from known respiratory ammonifiers and accompanying N-module composition for each organism. Pool quinone is also noted for dual-pathway nitrite reducers and model species. Colors of the main branches denote the 1st heme motif type: CxxCK and CxxCH. (B) Protein atomic composition for N and C normalized to protein length for NirK and NrfA nitrite reductases. (C) State-transition from ammonium-replete to ammonium-deplete for *I. calvum* C5 grown under 8mM lactate 12mM nitrate minimal media at 30 ºC. Metabolite profiles for ammonium-deplete are shown.

Figure 2. The effects of high resource (left; range of lactate concentrations with 12 mM NO_3^-) and low resource (right; range of lactate concentrations with 1.2 mM NO_3^-) concentrations with the same $C:NO_3^-$ ratio on pathway selection in *I. calvum* C5. (A) Production of N_2O-N and net change of NH_4^+ over a 100-hour incubation period at 30 ºC. Each bar represents the average of 8-10 replicates per treatment (Table S5). (B) Fraction of dissimilated N by pathway. (C) Growth rates for each corresponding treatment. The x-axis label defines lactate concentration and $C:NO_3^-$ ratio in parentheses.

Figure 3. (A) Time-series metabolite profiles for lactate, nitrate, and nitrite (top pane), production of dissimilated end-products as N_2O-N and net change in NH_4^+ ammonium production (middle pane), and corresponding growth curve of *I. calvum* cells grown under 8 mM lactate 12 mM nitrate ($C:NO_3^-$ ratio = 2) (bottom pane). Sampling points during growth phases are marked where transcriptomic profiling was performed (red arrows). (B) Metabolic reconstruction of the ETC from *I. calvum* with transcriptional changes for genes participating in dual-pathway dissimilatory nitrite reduction. Log_2 fold changes in transcript abundance are shown for late exponential relative to early exponential growth phase (EE vs. LE), stationary phase relative to early exponential growth phase (EE vs. ST), and stationary phase relative to late exponential growth phase (LE vs. ST). Locus IDs for each gene product correspond to heat map subplots in the order shown (left-to-right for each growth phase and top-to-bottom for each locus ID specified). Higher transcript abundance is represented in red, lower transcript abundance in blue, and no change in transcript abundance in white. Significant changes in transcript abundance ($p < 0.01$) are marked as a red box. Value of log_2 fold change is specified within each subplot. The log_2 fold changes of 14 NADH dehydrogenase subunits (Intca_03465-03530) were averaged as transcriptional changes were all shifted in the same direction.
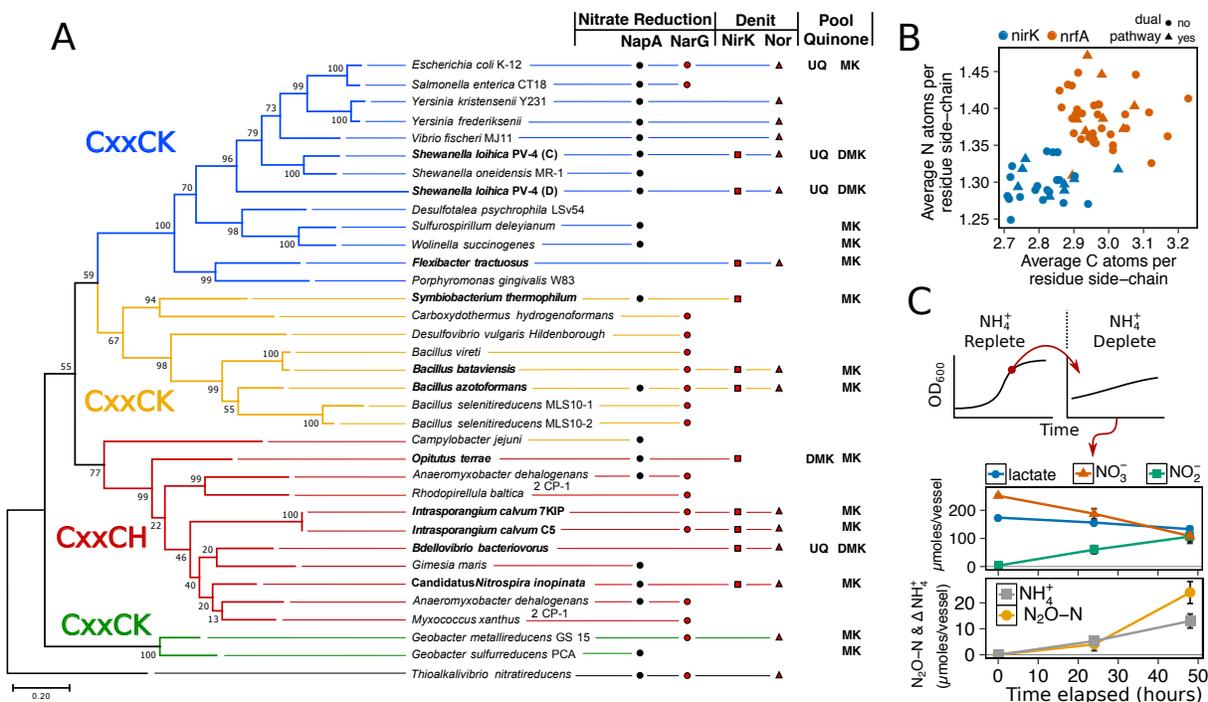
20

Figure 1. (A) Maximum likelihood phylogenetic tree of NrfA amino acid sequences from known respiratory ammonifiers and accompanying N-module composition for each organism. Pool quinone is also noted for dual-pathway nitrite reducers and model species. Colors of the main branches denote the 1st heme motif type: CxxCK and CxxCH. (B) Protein atomic composition for N and C normalized to protein length for NirK and NrfA nitrite reductases. (C) State-transition from ammonium-replete to ammonium-deplete for *I. calvum* C5 grown under 8mM lactate 12mM nitrate minimal media at 30 ºC. Metabolite profiles for ammonium-deplete are shown.
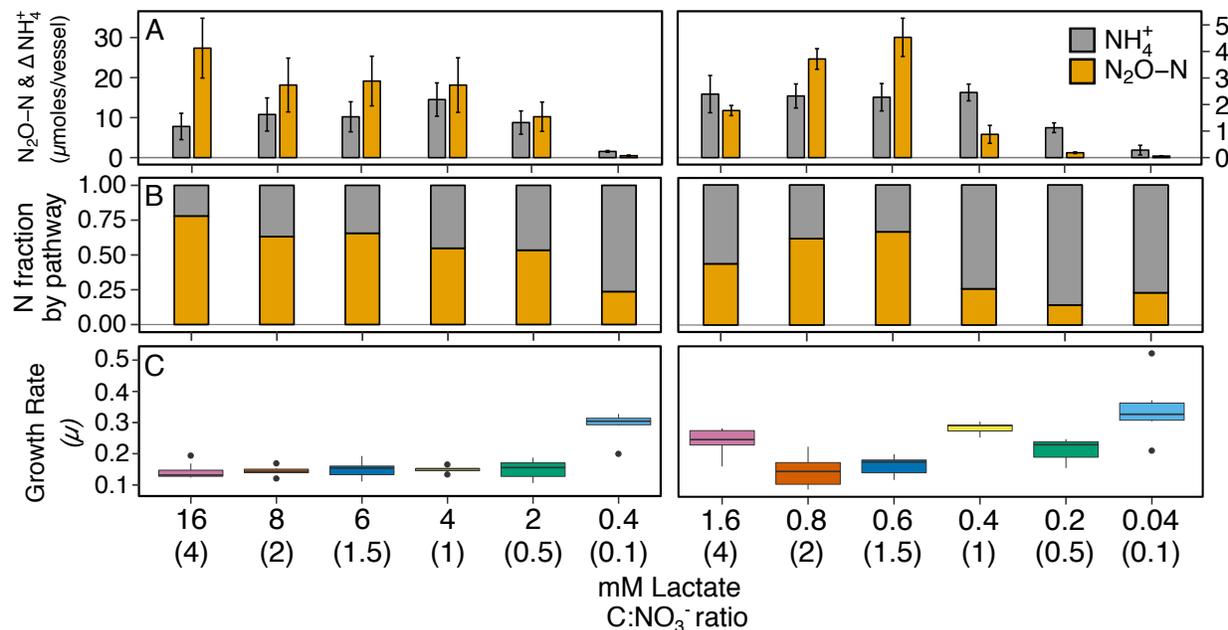
Figure 2. The effects of high resource (left; range of lactate concentrations with 12 mM NO_3^-) and low resource (right; range of lactate concentrations with 1.2 mM NO_3^-) concentrations with the same $C:NO_3^-$ ratio on pathway selection in *I. calvum* C5. (A) Production of N_2O-N and net change of NH_4^+ over a 100-hour incubation period at 30 ºC. Each bar represents the average of 8-10 replicates per treatment (Table S5). (B) Fraction of dissimilated N by pathway. (C) Growth rates for each corresponding treatment. The x-axis label defines lactate concentration and $C:NO_3^-$ ratio in parentheses.
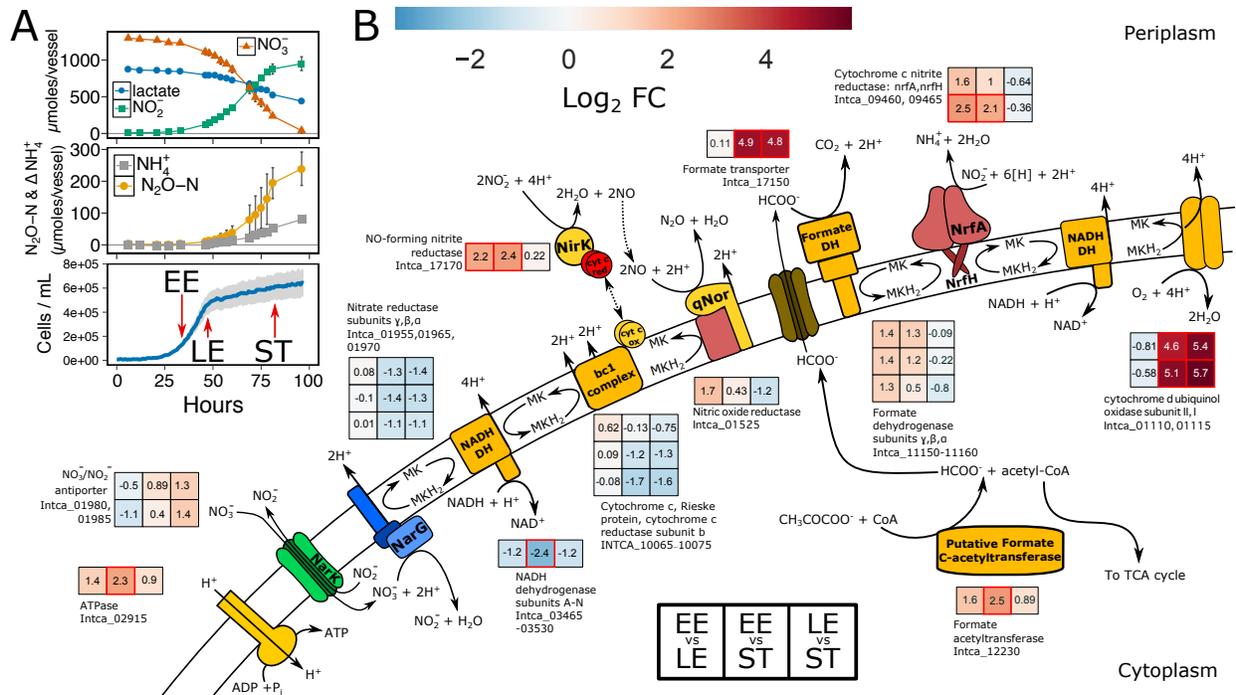
Figure 3. (A) Time-series metabolite profiles for lactate, nitrate, and nitrite (top pane), production of dissimilated end-products as N_2O-N and net change in NH_4^+ ammonium production (middle pane), and corresponding growth curve of *I. calvum* cells grown under 8mM lactate 12mM nitrate (C:NO_3^- ratio = 2) (bottom pane). Sampling points during growth phases are marked for transcriptomic analysis. (B) Metabolic reconstruction of the ETC from *I. calvum* with transcriptional changes for genes participating in dual-pathway dissimilatory nitrite reduction. Log_2 fold changes in transcript abundance are shown for late exponential relative to early exponential growth phase (EE vs. LE), stationary phase relative to early exponential growth phase (EE vs. ST), and stationary phase relative to late exponential growth phase (LE vs. ST). Locus IDs for each gene product correspond to heat map subplots in the order shown (left-to-right for each growth phase and top-to-bottom for each locus ID specified). Higher transcript abundance is represented in red, lower transcript abundance in blue, and no change in transcript abundance in white. Significant changes in transcript abundance ($p < 0.01$) are marked as a red box. Value of log_2 fold change is specified within each subplot. The log_2 fold changes of 14 NADH dehydrogenase subunits (Intca_03465-03530) were averaged as transcriptional changes were all shifted in the same direction.